Determining the Time Window for Dynamic Nanowire Cell Penetration Processes

Xi Xie,[†] Amin Aalipour,[†] Sneha V. Gupta,[‡,§] and Nicholas A. Melosh*,[†]

[†]Department of Materials Science and Engineering, and [§]School of Medicine, Stanford University, Stanford, California 94305, United States and
[‡]UCSF School of Pharmacy, Bioengineering and Therapeutic Sciences, University of California, San Francisco, San Francisco, California 94143, United States

ABSTRACT Nanowire (NW) arrays offer opportunities for parallel, non-destructive intracellular access for biomolecule delivery, intracellular recording, and sensing. Spontaneous cell membrane penetration by vertical nanowires is essential for these applications, yet the time- and geometry-dependent penetration process is still poorly understood. In this work, the dynamic NW–cell interface during cell spreading was examined through experimental cell penetration measurements combined with two mechanical models based on substrate adhesion force or cell traction forces. Penetration was determined by comparing the induced tension at a series of given membrane configurations to the critical membrane failure tension. The adhesion model predicts that penetration occurs within a finite window shortly after initial cell contact and adhesion, while the traction model predicts increasing penetration over a longer period. NW penetration rates determined from a cobalt ion delivery assay are compared to the predicted results from the two models. In addition, the effects of NW geometry and cell properties are systematically evaluated to identify the key factors for penetration.

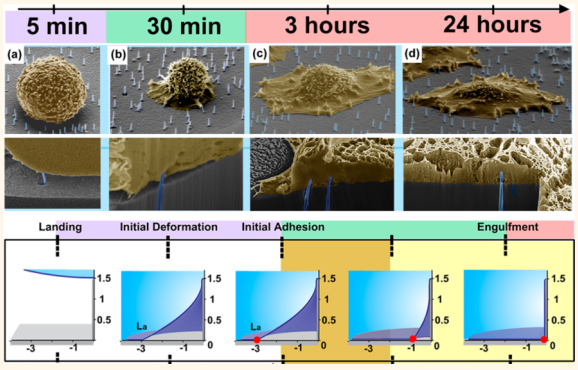

KEYWORDS: nanowire array · cell membrane penetration · cell adhesion · traction force · nanowire delivery

Recent advances in nanotechnology have stimulated development of novel nanomaterial platforms for biomedical applications by leveraging nanometer length scale fabrication to interface with subcellular features.[1−11] In particular, nanoscale structures such as nanotubes and nanowires (NWs) appear to penetrate cell membranes under certain conditions by creating localized stresses owing to their sharp features, which open up new opportunities to access the intracellular environment and manipulate living cells.[12−18] Compared to single-probe or single-cell platforms, seeding cells on top of NW arrays provides high-throughput delivery,[19−21] which has provided a powerful new modality for massively parallel biomolecule delivery,[22−27] intracellular electrical recording,[28−30] and intracellular enzymatic activity probing.[17]

Cell membrane penetration by vertically aligned NWs is the critical step for these important applications, yet the dynamic penetration process is poorly understood, and the experimental evidence for spontaneous penetration is still controversial. NW penetration into cells is indirectly supported by several delivery experiments.[22−26,28,31] For example, Shalek *et al.* delivered biomolecules into a broad range of cell types, including primary neurons and immune cells, which are difficult to deliver with other traditional techniques.[22−24] Chiappini *et al.* developed Si nanoneedle arrays that can provide access to cell cytosol and co-deliver DNA and siRNA.[31] However, other studies were unable to observe cell membrane penetration using microscopy techniques.[32−35] Although there are resolution limitations with these microscopy techniques, they are supported by electrical measurements, such as those by Xie *et al.*,[29] which showed that ∼150 nm diameter NW electrodes were consistently extracellular, requiring an electroporation pulse to gain access through the cell membrane. In addition, experimental evidence that cell morphology and division were perturbed by NWs over short time

* Address correspondence to nmelosh@stanford.edu.

Received for review April 7, 2015 and accepted November 11, 2015.

Published online November 11, 2015
10.1021/acsnano.5b05498

scales but returned to normal within a couple of hours[22] and that the membrane resealed after electroporation[29,36] suggests that the cell membranes can "heal" after the initial penetration events. This greatly complicates the visualization of penetration and makes the question of "when penetration occurs" significant in optimizing delivery strategies. Rational design of NW arrays for effective penetration thus requires understanding the dynamic penetration process and the governing factors of NW geometry and cell properties that determine membrane penetration.

Previous theoretical results examined the likelihood of cell penetration through a gravity-driven impaling mechanism or through adhesion forces.[37] However, these calculations were based on a static model that assumes the cell membrane adopts the minimum energy profile at infinite time. In reality, cell morphology is changing during dynamic spreading, motility, and adhesion,[38−43] during which the membrane undergoes viscous relaxation,[41,44−47] and continuously rearranges itself by active processes.[48,49] The cell membrane can adopt diverse profiles while interfacing with NWs during different cell adhesion and motility activities, in which case the penetration behavior may vary substantially. Therefore, the static model based on limited membrane profiles represents only one possible scenario of when penetration could occur and may miss dynamic processes.

In order to better understand the dynamic nature of cell penetration, we performed three studies. First, examples of typical cell morphologies on nanowire arrays were observed by focused ion beam milling and scanning electron microscopy (SEM) of cells cultured onto a nanowire array for different periods of time. This provides snapshots, albeit limited, of possible cell membrane shapes around the nanowires as they land and deform around the nanowires. Second, the number of cell penetration events was measured as a function of cell adhesion time using a Co^{2+} quenching assay. This provides direct experimental evidence for the time scale and number of penetration events per cell. Finally, two analytical mechanical failure models were developed based on the observed geometries and penetration results.

RESULTS AND DISCUSSION

Typical interface structures between cells and 100 nm diameter hollow NWs as a function of time after deposition were observed with the SEM. Hollow Al_2O_3 NWs were fabricated *via* a nanoporous template-based technique (Figure 1a, Supporting Information Figure S1.1).[11,25] Figure 1b−e shows SEM images of the cell−NW interface for Chinese hamster ovary cell spreading on an array of NWs. The 100 nm diameter, 1.5 μm high NWs with a density of 3×10^7 NW/cm^2 were coated with poly-D-lysine or fibronectin to promote adhesion. The initially spherical cell settles onto the NW array (0−5 min, Figure 1b), then gradually makes contact with the substrate and continues to adhere (∼5−30 min, Figure 1c). After the initial substrate contact, the cell continues to spread and increase its substrate contact area, corresponding to an intermediate phase of cell spreading (∼0.5−3 h, Figure 1d). During this period multiple cell extensions attached to the NWs are observed, and NWs are engulfed by the cell body. After several hours the cell reaches a late phase of mature adhesion (3−12 h, Figure 1e). Note that the exact timing of this process varied from cell to cell; thus the temporal range is fairly broad. The NW−cell interface cross sections were imaged using focus ion beam (FIB) milling (Figure 1f−j, Supporting Information Figure S1.2a and b). As shown in Figure 1g, cells with a 5 min culture time settled onto the NWs, but did not contact the substrate (indicated with black arrow). After 30 min, cell membrane developed focal adhesions to the substrate (Figure 1h), and the bottom of the cell membrane developed attachment to the substrate. NWs are observed to be in contact with the membrane, and the membrane is often slightly distorted around the NW, yet full engulfment is less common. After culturing for 3 h (Figure 1i), cells were in contact with the substrate and closely wrapped around the NWs. With 24 h culturing (Figure 1j), the cell interfaces were found to be similar to those observed at 3 h, but with cell spreading over a larger area. On fully spread cells (Figure 1k), the cell membrane often forms a "tent"-like structure above the NWs (red arrows), while the cell membrane near the cell periphery grasps onto the NWs (blue arrows). The general shape and temporal progression of the cell−NW interfaces was consistent over multiple experiments, yet it is important to note that some cell damage does occur during the fixation, drying, and ion milling; thus detailed analysis of the nanoscale membrane structure should not be made based on these experiments alone (Supporting Information Figure S1.2). These results are also consistent with several other microscopy observations that the cell membrane often completely deforms around the NWs after an extended culture period.[32,33,37,50]

The number of NWs that actually penetrate the cell membrane (rather than cell engulfment) was determined by a recently developed cobalt ion (Co^{2+}) delivery assay.[51] In this technique, the hollow NWs are used to deliver Co^{2+} to CHO cells expressing green fluorescent protein (GFP). If the NWs penetrate the cell membrane, cobalt ions diffuse into the cytosol and quench the intracellular GFP fluorescence, forming distinct quenching spots (Figure 2a). Each spot corresponds to a penetration event, which can be readily quantified using fluorescence microscopy. The number of penetrating events can be converted to the percentage of NWs based on the known number of

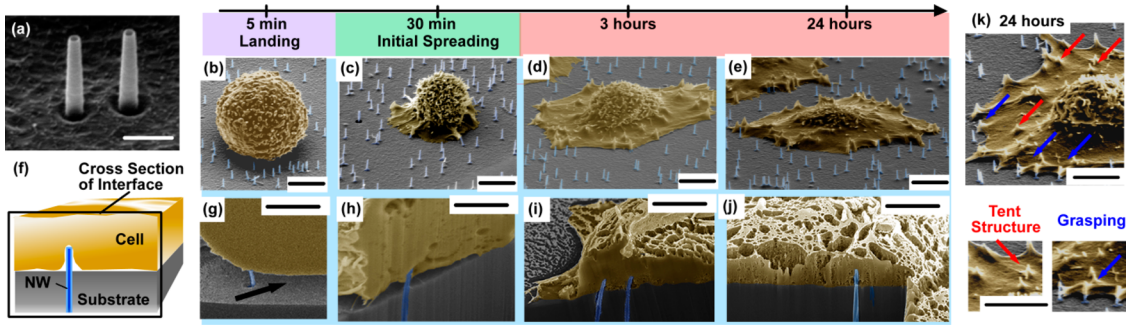

Figure 1. (a) SEM image of hollow alumina NWs. Scale bar: 400 nm. (b−e) SEM images showing CHO cell spreading on NWs (b) 5 min, (c) 30 min, (d) 3 h, and (e) 24 h after cell plating. Scale bar: 5 μm. (f) Illustration and (g−j) SEM images of NW−cell interfaces further revealed with FIB milling. Scale bar: 2 μm. (k) The cell membrane appears to form a tent structure above the NWs (indicated with red arrows) or grasping onto NWs near the cell periphery (indicated with blue arrows). Scale bar: 2 μm.

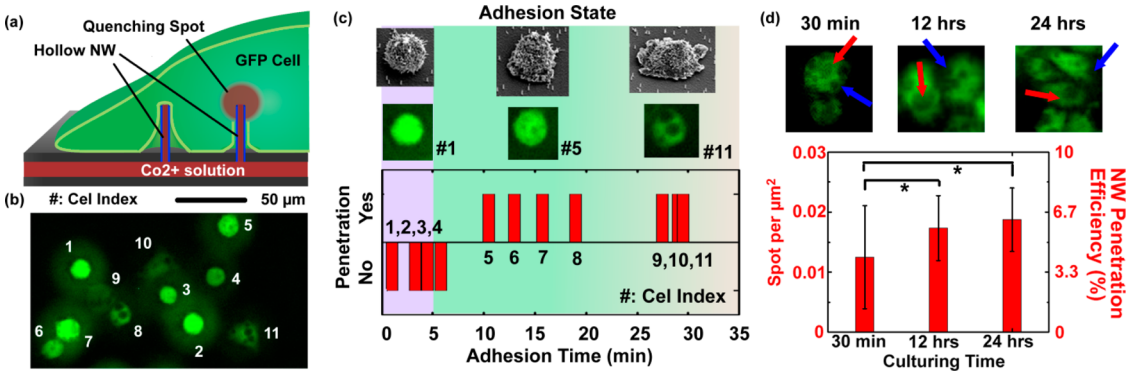

Figure 2. (a) Illustration of hollow NW-mediated Co^{2+} delivery assay. If the hollow NWs penetrate the cell membrane, Co^{2+} would diffuse into the cytosol and quench the intracellular GFP fluorescence, forming distinct quenching spots. (b) Fluorescence image showing quenching spots observed distinctly in a spread cell when Co^{2+} pulses were added at 30 min after cell plating. Each cell was identified with an index number. (c) Analysis of the penetration state and adhesion state of each cell shown in (b). Distinct step function in penetration occurs after 5 min. (d) Quenching spot density and NW penetration yield at different cell culture time points (30 min, 12 h, and 24 h, 50 cells were counted for each group) were analyzed based on a Co^{2+} delivery assay. * indicates statistical significance at the level of $p < 0.005$ using Student's test. Noted that the quenching spots appear on both the cell's central area (red arrows) and the cell peripheral area (blue arrows).

NWs per unit area. Cell penetration at the various cell culture time points was assessed using this technique. Cells in suspension were deposited onto the NW array, and the time at which each cell landed upon the NW array was recorded (Figure 2b and c). A Co^{2+} pulse (500 mM) was applied underneath the NW substrate at 30 min, and successful penetration was determined by observation of at least one quenching spot within a cell (Supporting Information Figure S1.3). As an example, Figure 2b shows 11 such cells (more analysis on 70 cells can be found in Supporting Information S1.4), each identified by a unique index number. The time that each cell landed on the substrate and the total cell culture time on the NW array before the Co^{2+} injection were recorded for each cell (Figure 2c). Cells that had been in contact with the substrate for the longest (cells #9, #10, and #11) spread over the largest area, while cells that only recently landed on the substrate were less well spread (cells #1, #2, #3, and #4). Quenching spots were observed most commonly in those cells that had adhered the longest (adhesion time >18 min, cells #8, #9, #10, and #11), while cells that most recently landed on the substrate (adhesion time <5 min, cells #1, #2, and #3) show no quenching spots. A step function in penetration occurs at roughly 5 min, coinciding with cell contact to substrate and spreading from the SEM study (Figure 2c). The percentage of NWs penetrating cells was estimated based on the measured number of spots per area and the known number of NWs per area. When the data are compiled from all the cells in the sample, the total number of penetration events per cell over time is roughly sigmoidal, with the percentage increasing rapidly from 5 to 30 min, then slightly increasing from 30 min [0.012 ± 0.009 spots/μm^2 or $\sim(4.2 \pm 2.9)$% NWs] to 12 h [0.017 ± 0.005 spots/μm^2 or $\sim(5.8 \pm 1.8)$% NWs], finally reaching a plateau between 12 and 24 h [0.019 ± 0.005 spots/μm^2 or $\sim(6.2 \pm 1.8)$% NWs] ($n = 50$ for each sample). Penetration was observed on both the cell's central region (red arrows) and cell periphery (blue arrows). While representative areas of cells were chosen for these figures, the statistical information was derived from a much larger population of cells and is consistent with the results shown (Supporting Information S1.5).

Inspired by these experimental observations, we constructed two mechanical models to understand the NW cell penetration process during cell spreading. In the first model, the cell membrane is assumed to form a symmetric tent configuration around the NWs, where penetration occurs due to cell−substrate adhesion forces, noted as the "adhesion model", representative of NWs located under the cell body. The second model assumes the cell membrane asymmetrically grasps onto NWs, where penetration occurs under cellular traction force, noted as the "traction model". These two cases were the most common features observed when the initial penetration events occurred, thus are considered likely candidates for penetration geometries. The mechanical difference between the two is the degree to which the nanowire is engulfed and the directionality of the force. The cell membrane is treated as an isotropic elastic sheet, which encompasses mechanical properties of both the lipid bilayer and the basal cytoskeleton.[37,52−55] An intermediate value for the membrane Young's modulus (E) of 48 MPa is chosen,[37] although values ranging from 10 to 200 MPa have been reported for different cell types.[52,56−58] Cell membrane rupture is determined based on activation energy theory, where penetration is defined to occur once the membrane tension reaches critical tension T^* = 5.6 mN/m (Supporting Information S2).[37] Experimentally this value is in the range 1−10 mN/m, dependent on the membrane strength. The effect of this choice is evaluated later in our analysis.[59,60]

In the adhesion model, the cell lands on a single NW under gravity, and the cell membrane periphery makes contact with the substrate at an assumed position L_0 at the initial time point t_0 to establish the initial adhesion. After this adhesive contact, the cell−substrate adhesion force encourages additional membrane−substrate contact, which leads to evolution of cell membrane deformation until it eventually reaches the NW surface (Figure 3a). To model this scenario, penetration was determined at a series of snapshots of a given membrane configuration, in order to evaluate membrane penetration at each membrane contact position. At each moment the membrane profile and force distribution are evaluated independently from the previous moment.

The shape of the membrane around the NW is calculated for a sequential series of deformations after initial contact using the mathematical formalism of clamped membrane indentation under the loading of a net vertical force (Supporting Information S3).[37,61] On the basis of an axisymmetric solution of the meridian and circumferential displacements, the membrane profiles are numerically computed by minimizing strain energy under the boundary condition of zero displacement at substrate contact points, in which the membrane's strain energy is described by a Mooney strain-energy function assuming the cell membrane is isotropic and incompressible.[53,54] The initial contact profiles are determined by calculating the shape of the membrane when it settles on the substrate assuming a typical 10 pN buoyancy force on the cell (Supporting Information S4).[37]

At each time $t(i)$ (or equivalently the cell periphery's position $L(i)$), the membrane−substrate interaction creates a vertical adhesion force that leads to tension on the membrane, which can cause penetration when the tension at a given point in the membrane exceeds the threshold failure value of 5.6 mN/m. The component of the adhesion force in the normal direction (F_n) is calculated by integrating the adhesion tension along the contact circumference (Figure 3b):[37]

$$Fn(i) = 2\pi L(i) \times \gamma \times \sin[\theta(i)] \quad (1)$$

where γ is the membrane−substrate adhesion surface tension in proportion to the adhesion energy density (W), which is assumed to be a constant and distributed uniformly around the contact circumference.[62,63] Cell adhesion energy density (W_a) is normally on the order of $(1-10) \times 10^{-5}$ J/m^2 [38,63] and is assumed to be 3×10^{-5} J/m^2 here, corresponding to an adhesion tension of 0.5 mN/m (Supporting Information S2).[41,64] The contact angle θ is formed between the membrane and substrate, the contact length L is the distance between the membrane−substrate contact points and the NW, and the NW spacing D is defined to be the shortest distance between two neighbor NWs. The maximum value of L is assumed to be one-half of the NW spacing (Supporting Information S5).

To illustrate the penetration process as a cell adheres to an NW array, we considered a cell deforming around a single NW (R = 50 nm, H = 1.5 μm, and D is infinite for a single NW). As shown in Figure 3c, upon landing on the NW, the cell deforms around the NW with a contact length L_0 = 2.9 μm (blue) at $t = t_0$. Following this initial contact phase, the cell generates adhesive contacts to the surface, creating an adhesion tension of γ, causing the cell membrane to spread on the substrate and deform toward the NW. After the initial contact at position L_0, the vertical adhesion force (F_n) decreases with time (0−2.5 nN, as shown with a red curve in Figure 3d). This is because the decreasing contact length (L) gives a smaller circumference of membrane−substrate contact to generate vertical adhesion force, although this is slightly offset by the increasing contact angle. Once L is less than L^* = 0.9 μm (corresponding to a critical time point $t = t_0 + t^*$), the adhesion force becomes insufficient to induce penetration. Therefore, the range between L_0 and L^* (or t_0 and $t_0 + t^*$) defines the penetration regime (yellow, Figure 3c and d). This result suggests why the observed penetration events plateau after an extended period of time; once the cell closely engulfs the NW, it no longer creates the stress necessary to cause membrane failure.

The width of the penetration regime $L_0 - L^*$ (or t^*) is thus a strong indicator of the penetration likelihood.

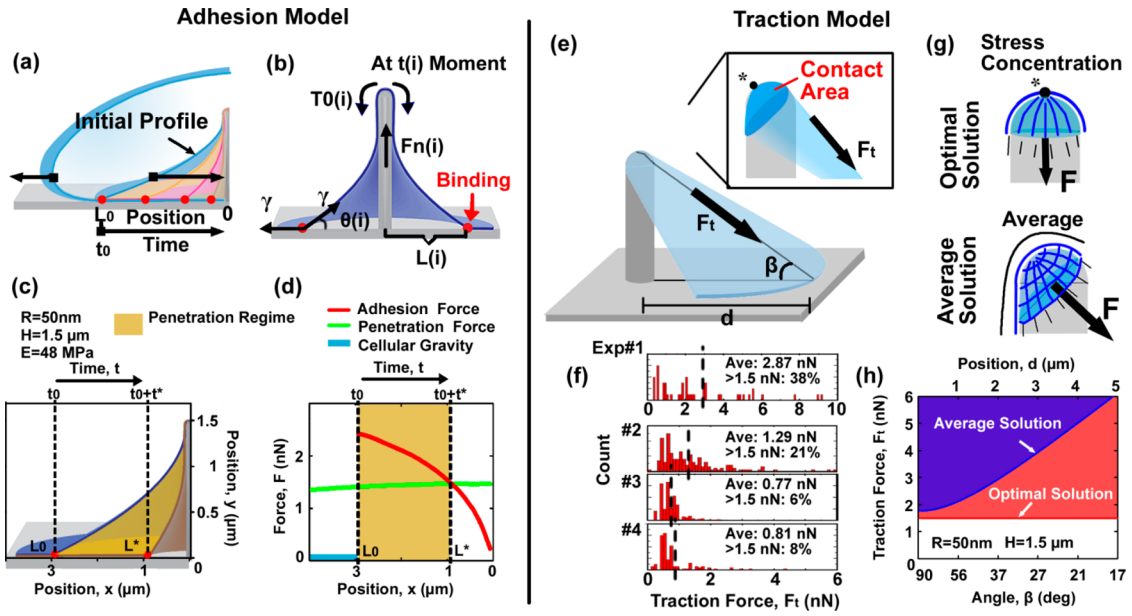

Figure 3. (a–d) Adhesion model. (a) The scenario of the adhesion model. The cell membrane subsequently deforms around NWs under cell–substrate adhesive interactions. The membrane periphery initially contacts the substrate at a position L_0 and starting time point t_0. The cell membrane then gradually deforms until completely engulfing the NW. (b) Schematic of the calculation of vertical adhesion force, which is dependent on membrane–substrate contact and cell adhesion. (c) Results of the penetration regime (yellow regime) and (d) corresponding force analysis when the cell deforms around a single NW (R = 50 nm, H = 1.5 μm) based on the adhesion model. (e–h) Traction model. (e) Schematic of the traction model and force analysis. (f) The range of traction forces were analyzed based on previously reported nanopillar-deflection experiments. The analysis is discussed in Supporting Information Figure S6.1. (g) Schematics of the evaluation of the optimal and average solutions for membrane penetration as a function of applied force. (h) Result showing the penetration regimes based on the traction model, calculated with both optimal (red) and average (blue) solutions.

For a narrow regime, cell penetration is likely to occur only within a short period after contact, and further penetration becomes difficult once the cell membrane begins to deform closer to the NW. In addition, if the penetrated membrane is able to reseal, as observed in electroporation experiments,[29] penetration would rarely occur a second time because the plasma membrane may have already wrapped around the NW and reduced the membrane tension such that it cannot induce a new penetration.

While the adhesion model treated the case of the cell isotropically "tenting" around the nanowire, another likely penetration scenario is during cell traction and motility. In the traction model a cell section such as a lamellipodia grasps the NWs and exerts an anisotropic traction force that induces tension on the cell membrane. This could also occur if the stress is anisotropically distributed under the cell body. The leading edge of cell extension is assumed to wrap around the NW, as observed from the electron microscopy images, and produces a unidirectional force (Figure 3e). This directional force causes the cell to deform into an asymmetric cap geometry (highlighted with darker blue), where the contact boundary is assumed to be in a plane perpendicular to the force along the cell section surface. The cell section pulls against the NW, making an angle β between the substrate and the NW contacts, where β can vary from 90° for a purely vertical force to 0° for a completely lateral force. Traction force (F_t) in the cell section is directed along the cell membrane between the substrate and NW tip.

An important parameter for the likelihood of penetration is the magnitude of the cell traction forces along these extensions. Cell pulling forces have been reported in the range 0.1–10 nN,[65–68] yet the force distribution can vary between different measurement techniques and experimental conditions. The exact force magnitudes when cells pulled against the NWs in our system are still lacking. Here we choose representative cell traction forces measured from cell traction force studies based on micropillar or nanowire displacement.[67,68] The distribution of the traction forces observed from these experiments is plotted in Figure 3f (Supporting Information Figure S6.1). The majority of the traction forces are less than 1 nN; however forces as large as 5 nN were also observed, although not in great number (<10%). Given that only ~6% of the NWs in our experiments are observed to penetrate the cell membrane, we conservatively take the upper ~10% tail of forces (between 1 and 5 nN) as the cell's pulling force acting on the NWs that induce penetration.

It is important to note that any model of a system as diverse and complicated as a cell extension wrapping around a post is going to be an oversimplification of the actual geometry. In order to combat against bias due to selection of a particular geometry, we analyze

two extreme cases for the force loading conditions. In one case (the "optimal" case) that force is loaded uniformly around the NW, allowing maximum stress concentration at the tip. This results in the lowest stresses required to rupture the membrane (Figure 3g).

In this scenario, all the applied force contributes to the tension at the tip apex, which has a very small surface area and thus maximal stress concentration. This was calculated by the hemispherical tip-indentation model, which reduces to the same "tent" scenario used for the adhesion model. As opposed to the tip-concentration model, we assume there is no stress concentration at all in the "force-averaged" solution, and instead the stress is averaged over the entire membrane−NW contact area, with the sum of the forces equal to total applied force (Supporting Information Figure S6.3). In this case the stress is inherently less than any models with stress concentration, thus least likely to induce penetration. While it is possible to find systems with even lower stress on the NW (*e.g.*, a stress fiber running parallel to the NW), these are not treated, as the required forces rapidly become quite large and do not agree with experimental observations.

Here we compare our calculation results with representative cell traction forces measured from several works that studied a cell's pulling force on nanowires or micropillars. Figure 3h shows the estimated penetration regime (colored) for cell geometries with different contact distances (or angle β) from the NW (R = 50 nm, H = 1.5 μm), calculated with both the optimal and average solutions. In the optimal solution (red regime), penetration is estimated to occur around 1.5 nN and largely independent of contact distance in the range 0−5 μm. For the average solution (blue regime), the necessary penetration forces are higher (1.7 nN at 90° contact angle) and highly dependent on traction angle. For cell sections with very high attachment angles (∼90°), the two solutions are similar. However, for lower contact angles the required force rapidly increases. The required traction force for penetration is estimated in the range of 1.5−6 nN over the angle range of 17°−90°. Comparing this to the observed traction forces in Figure 3f, roughly 6, 8, 21, or 38% (in varying measurements) of the cell's traction force would fall within this range. These results suggest that cell penetration under traction force is likely for the observed upper range of traction forces, but is quite rare for lower forces. Note that these results predict penetration due to cell traction is favorable for longer cell adhesion times and thus more vertical NW−membrane contact angles, opposite from the tent-adhesion model.

Based on the above results, a schematic of a hypothetical penetration process combining adhesion model and traction model is described in Figure 4. From t = 0 to t_0, the cell lands on the NW array under gravity, making initial contact with the substrate. This period is the early phase of spreading, which generally takes ∼0−10 min based on experimental observations. Little penetration would occur during this period since the cellular gravity and nonspecific cellular forces are generally too weak to induce cell membrane rupture.[37] After the establishment of initial adhesion, the cell membrane continues to deform around the NW, increasing its substrate contact area. From t_0 to $t_0 + t^*$, corresponding to the intermediate spreading phase shortly after initial adhesion formation, penetration is most likely to occur based on the adhesion model (dark yellow color). This prediction is consistent with experimental evidence that cell penetration is normally observed to occur in the early cell culture period (∼0.5 h) after plating.[22,23] At the same time the cell membrane keeps deforming and wrapping around the NW, weakening the potential of NW penetration under adhesion force. After $t_0 + t^*$, the NWs are closely engulfed by the cell membrane, and new penetration is unlikely to occur by cell adhesion. In the meantime, cell traction forces during cell spreading may also introduce some penetration over a longer culture period, increasing the total penetration yield. The adhesion model predicts a limited time window for penetration during initial cell spreading, while the traction model suggests penetration is more likely to occur after longer contact time when the cell membrane subsequently advances near the NWs, making a higher angle β. Since very little new penetration is observed after the first several hours, while cell extension and protrusions are still observed over the entire period, it appears that the tent-adhesion mechanism may be the most likely candidate.

After establishing the penetration process, the model is applied to predict design rules for penetration by considering varied NW geometry or cell properties (Figure 5a): NW radius (R), NW height (H), NW array spacing (D), cell adhesion (W), cell stiffness (E), and the criteria for membrane rupture (T^*, inversely related to membrane strength). Since the adhesion model and the optimal solution of the traction model both reduce to the hemispherical membrane cap model, here we evaluate the design rules based on the adhesion model. To elucidate the design rules, the maximum NW radius for penetration (defined as the critical radius) was plotted as a function of the other NW properties or cell properties, where a larger NW radius indicates lower penetration capability. The colored regimes in Figure 5b−g indicate the feasible conditions to achieve penetration, with the NW radius ranging from 10 to 200 nm (Supporting Information S8).

First the effects of NW spacing in an array are evaluated. As shown in Figure 5b, for three typical NW heights (0.5, 1.5, and 2.5 μm), the critical radius to induce penetration initially increases with increasing NW spacing. This is expected since reduced spacing limits the cell−substrate contact, thus providing less vertical adhesion force for penetration, while increased spacing releases this contact limitation. As NW spacing

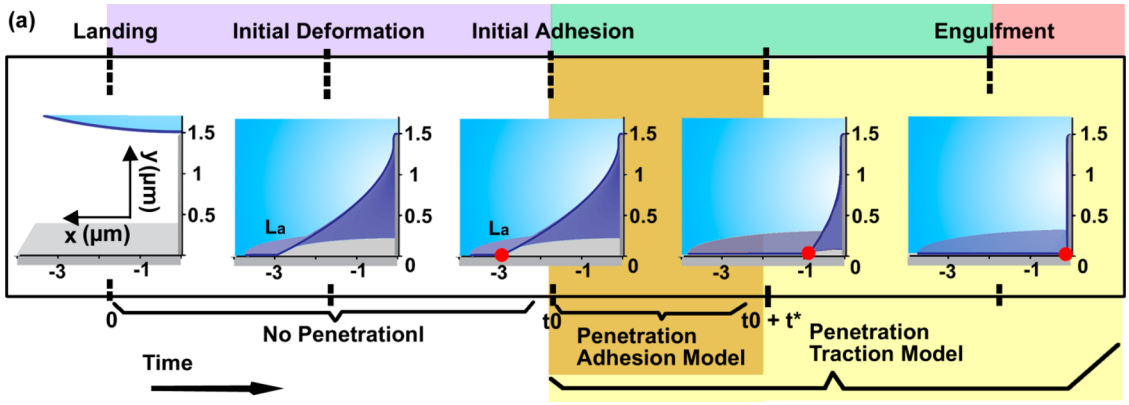

Figure 4. Illustration of the penetration process. The NW radius is 50 nm and the height is 1.5 μm. From $t = 0$ to t_0, the cell lands on the NW under gravity, making initial contact with the substrate, followed by initial adhesion formation at t_0. From t_0 to $t_0 + t^*$ (dark yellow), penetration is mostly likely to occur based on the adhesion model. In the mean time, cell traction force may still introduce some penetration over a longer culture period.

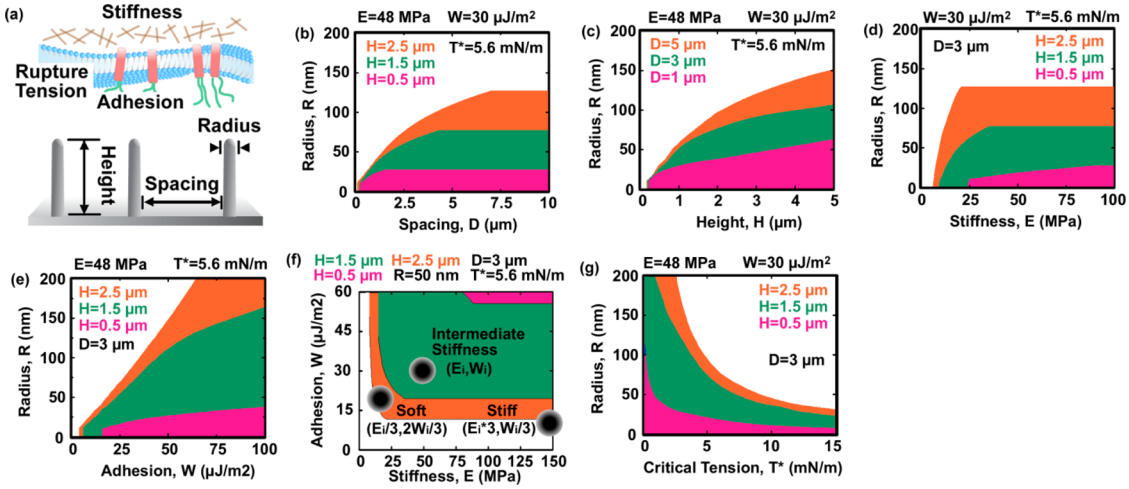

Figure 5. (a) Illustration of the six factors considered in the design rule on NW penetration. (b−g) Effects of (b) NW spacing (D), (c) NW height (H), (d) cell stiffness (E), (e) cell adhesion (W), (f) cell types, and (g) membrane failure tension (T^*) on penetration. The colored regimes indicate the feasible NW radius (in the range 10−200 nm) to induce penetration.

increases further, the effect of NW spacing reaches a maximum plateau. This transition occurs because the cell−substrate contact is also limited by the initial contact distance (L_0) when the cell membrane initially makes contact with the substrate at $t = t_0$ (Supporting Information S5). The cell−substrate contact saturates to this limit as NW spacing increases beyond the critical distance. The position of the plateau depends on the NW height, with the plateau appearing earlier with shorter NWs than longer NWs. These results suggest that larger NW spacing is favorable for the penetration of individual NWs into cells. However, for certain applications, the total number of NWs that penetrate into a cell is the important criterion, which implies that increasing the NW density is desirable. From this perspective, the selection of NW spacing should be ideally near the inflection points of the plateaus shown in Figure 5b.

Conversely, the effects of NW height at different NW spacing (D = 1, 3, and 5 μm, Figure 5c) are evaluated. The critical NW radius to induce penetration at different NW spacing (D = 1, 3, and 5 μm, Figure 5c) increases quickly with increasing NW height initially in the short NW range (<1 μm), followed by a slower rate of increase in the intermediate to long NW range (>1 μm). For example, in a 3 μm spacing NW array, short NWs with H < 0.5 μm limit penetration greatly, as only NWs with a radius of less than 27 nm can achieve effective penetration for this range of heights. As the height increases to 1.5 μm, the critical NW radius threshold increases to R = 67 nm, but a further increase of height to 5 μm improves this R threshold only to 107 nm. In addition, the critical radius to induce penetration increases with increasing NW spacing from 1 to 5 μm. Overall, the longer NWs are desirable for penetration purposes. However, it should be noted that in reality very long NWs may prevent cells from even making contact with the substrate especially for stiff cells. In this case the penetration mechanism may occur through a gravity-driven impaling mechanism,[37] which is discussed by the previous theoretical model.

After evaluating the effects of NW geometry on penetration, the influence of cell stiffness on penetration is investigated in Figure 5d. As a trend, the critical radius increases as cell stiffness increases and then reaches a maximum plateau. For example, in an array with $H = 1.5\ \mu$m and $D = 3\ \mu$m, the critical R rises from 11 to 77 nm with stiffness increasing from 10 to 35 MPa and reaches a plateau at $R = 77$ nm as $E > 35$ MPa. This is because the softer cells would have already heavily engulfed NWs even before making initial contact with the substrate, in which case the penetration potential is low. As cell stiffness increases, the membrane deforms with the initial contact points further from the NW, increasing the contact circumference and generating stronger adhesion force, which explains the enhanced penetration on stiffer cells. However, the membrane−substrate initial contact is also limited by the NW spacing, illustrated by $D = 3\ \mu$m in Figure 5d (Supporting Information S5). In the case of $H = 1.5\ \mu$m, as stiffness reaches 35 MPa, the initial contact reaches the limit set by the spacing $D = 3\ \mu$m; hence the critical NW radius reaches a plateau. In addition to the discussion in Figure 5d, there are three points that should be noted on the effect of cell stiffness. First, here it is assumed that the cells can actively reorganize and relax their cytoskeleton and membrane, allowing the membrane to eventually contact the substrate, regardless of the NW height or cell stiffness. In reality, this process is likely to be different for different stiffness cells, with highly rigid cells taking a much longer period for the membrane to relax and make substrate contact. Effectively this can be modeled by changing the starting time point of the intermediate spreading phase t_0 to a later time for stiff cells compared to soft cells. On the other hand, it might be expected that as cell stiffness reaches a certain level, the stiff cells may only sit on top of the NWs without contacting the substrate for an infinite time,[37] in which case no adhesion-mediated penetration would actually occur. Second, many stiff cells have very weak adhesion properties,[38] while here it is simply assumed that these cells have the same adhesion properties as the softer ones. Note that here the cell membrane penetration criterion is derived from the failure of the lipid bilayer and is assumed to be the same for different cell types. In reality, additional effects such as the cytoskeleton of different cell types may complicate the failure conditions.[55]

The effects of the strength of cell adhesion are evaluated in Figure 5e for a typical NW array with 3 μm spacing. The critical NW radius increases in a near-linear manner with the enhancement of adhesion strength from $W = 0$ to 100 μJ/m^2. This suggests the important role of substrate adhesion on penetration, consistent with recent experimental results that penetration efficiency can be greatly increased by employing adhesion-promoting molecules to enhance cell adhesion.[51] The use of thin NWs or low NW density can improve penetration yet presents a trade-off in real applications because these strategies achieve effective penetration by sacrificing the size and scale of NWs. On the other hand, cell adhesion properties can be altered by modifying the substrate surface coating with polylysine, fibronectin, laminin, and other adhesion-promoting molecules without limiting the geometry of NWs,[51] which provides a promising way to enhance penetration without significantly altering the NWs.

The penetration behavior of several specific cell types was evaluated by studying representative cell models with different cell stiffness and cell adhesion (Figure 5f, Supporting Information Figure S8): a soft cell ($E = E_a/3 =$ 16 MPa and $W = W_a/2 = 20\ \mu$J/m^2), a cell with intermediate stiffness ($E_a = 48$ MPa and $W_a = 30\ \mu$J/m^2), and a stiff cell ($E = E_a \times 3 = 144$ MPa and $W = 2W_a/3 = 10\ \mu$J/m^2). It was found that the cells that possess intermediate levels of membrane stiffness and adhesion are readily penetrated by a typical NW array with 50 nm NW radius and 3 μm NW spacing. On the other hand, softer cells and stiffer cells with weaker adhesion have less overlap with the penetration regimes, indicating limited penetration likelihood. These results suggest a large variation of penetration yield for different cell types.

Finally we evaluate how the choice of critical membrane failure tension (T^*) affects the penetration prediction.[59] From Figure 5g, in the regime of higher membrane strength ($T^* > 15$ mN/m), penetrations require the use of very thin NWs, *e.g.*, $R < 22$ nm, for NW height = 1.5 μm and spacing = 3 μm. This may model the condition of a cell type with high lipid membrane strength or of a cell where the basal cytoskeleton complicates the insertion of NW tips through the plasma membrane.[55] On the other hand, in the regime of lower membrane strength ($T^* < 2$ mN/m), the NW radius can take a very wide range of values ($R > 150$ nm), implying that the NW geometry is less critical. This may mimic conditions where some external poration techniques (*e.g.*, electroporation, chemical poration, external force, or NW surface functionalization) are applied to lower the membrane failure threshold.[69] By using these techniques, penetrations can be more easily achieved, yet there is concern over cell viability due to the invasive nature of these techniques.[11,27]

It is important to note that several other factors may come into play during the dynamic spreading process that could alter the results. In these models the dynamic penetration process was calculated based on a series of membrane profile snapshots, and the cell properties were assumed to be constant during the active cell adhesion and spreading process. However, cell adhesion involves a series of active cellular biological events; the focal adhesion formation is dynamic and cell properties may vary significantly during different adhesion states, and the role of the cytoskeleton is still not understood. These factors may further complicate the effectiveness of forces acting on the

cell membrane. In addition, this work is based on a continuum elastic membrane model that assumes the load-bearing elements are infinitesimally small. In reality the cellular forces are transmitted by the discrete elements of the cytoskeleton, and the continuum mechanical model becomes suspect as the nanowire diameter approaches the mesh size of the cytoskeleton. However, AFM measurements of cell penetration force by Angle *et al.*[70] comparing very sharp, 10 nm diameter tips and 200 nm diameter tips found differences between the two as would be expected based on the effective contact area, yet there was not a step-function-like change that would imply a transition to a submesh size regime. This suggests that the homogeneous treatment of the membrane used here is not unreasonable for typical NW diameters in the 50−250 nm range.

CONCLUSION

In summary, in this work the dynamic interfaces and penetration as cells adhere on a vertical NW array were studied with the electronic microscope, Co^{2+} delivery assay. Inspired by these experimental observations, two continuum mechanical models were developed to explore possible cell penetration processes. The adhesion model implies that spontaneous cell penetration by nanowires is possible, but should be observed only over a limited time window. The traction model suggests cell penetration occurs more often at greater NW engulfment, but only a few percentage of traction forces are sufficiently high to induce penetration. These results suggest that NW cell penetration is possible, yet limited in scope, time scale, and cell types. Aside from cell adhesion and traction forces, additional external forces or poration techniques may further enhance penetration for delivery applications. We believe this increased understanding of the dynamic cell penetration process, as well as the nanomaterial characteristics and cell properties that influence cell penetration, will be of significant importance toward the success of designing a new class of cell-interfacing tools to manipulate and measure intracellular activities.

METHODS

Nanowire Array Fabrication[11,25]**.** As illustrated in Supporting Information Figure S1.1, track-etched polycarbonate membranes (Maine Manufacturing, pore density 2×10^7 pores/cm^2, pores size 100 nm) were uniformly coated with 20 nm thick aluminum oxide by atomic layer deposition (ALD, $AlMe_3$ (TMA), H_2O, Cambridge Nanotech). A 200 total of pulse cycles (alternating $AlMe_3$ and H_2O pulses) of 0.015 s (precursor exposure time), 60 s (waiting time), and 60 s (purge time) were used to coat the high aspect ratio nanopores with conformal alumina coverage. In the second step, alumina on the top surface of the polycarbonate membrane was selectively etched by a dry ion etcher (Pquest), using 30 sccm BCl_3, 40 sccm Cl_2, and 5 sccm Ar at ECR 300 W and RF 60 W. In the third step, the polycarbonate membrane was selectively etched in a dry ion etcher (Pquest) again to expose the resultant nanowires, using 30 sccm O_2 at ECR 200 W and RF 60 W.

Cell Culture. The NW arrays were cleaned with O_2 plasma, then incubated with poly-D-lysine or fibronectin solution for 4 h. After rinsing with deionized water three times and cell medium one time, Chinese hamster ovary (CHO-K1) cells were plated onto the NW array and incubated at 37 °C and 5% CO_2. Cell medium consists of 90% DMEM supplemented with 9% fetal bovine serum and 1% antibiotics (penicillin−streptomycin).

SEM Imaging. Cells were cultured on NW arrays for 5 min, 30 min, 3 h, and 24 h. Then the cell samples were fixed with 2% glutaraldehyde solution for 10 min, followed by washing 3× in cacodylate buffer at pH 7.4. The cell samples were then stained with osmium tetroxide to improve contrast. The cell samples were gradually dehydrated with increasing concentrations of ethanol (0%, 30%, 50%, 70%, 90%, and 100%) and finally prepared by a critical point drying process. Samples were sputter-coated with gold−palladium and imaged in a SEM (Sirion). The cell−NW interface was further revealed with focused ion milling in a focused ion beam microscope (Helios FIB).

Delivery Assay. The as-fabricated hollow NW array was integrated with a microfluidic device that was prepared by assembling the NW array with a PDMS layer containing a microfluidic channel. The PDMS layers were prepared with PDMS elastomer and cross-linker (Sylgaard 184, Dow Corning), and the microfluidic channel was defined using a mold made with SU-8 photoresist. For delivery experiments, a Co^{2+} solution (500 mM) was pumped at 0.1 mL/h using a syringe pump.

Calculations Methods of Adhesion Model and Traction Model. The calculation methods are described in Supporting Information S3−S7.

Conflict of Interest: The authors declare no competing financial interest.

Supporting Information Available: The Supporting Information is available free of charge on the ACS Publications website at DOI: 10.1021/acsnano.5b05498.

Additional experimental details, experimental methods, calculation methods, supplemental figures, supplemental discussion, and table of abbreviations (PDF)

Acknowledgment. The authors wish to thank Alexander M. Xu for his help with Co^{2+} delivery experiments and the discussion of the models, Dr. Matthew R. Angle for his help with FIB experiments, and the Yi Cui and Sarah Heilshorn laboratories for use of equipment and experimental advice. This work was supported by a Stanford BioX-Neuroventures and NeuroFab Award (N.M., A.A., X.X.) and Human Frontiers Science Program RGP0048.

REFERENCES AND NOTES

1. Lieber, C. M. Semiconductor Nanowires: A Platform for Nanoscience and Nanotechnology. *MRS Bull.* **2011**, *36*, 1052–1063.
2. Yang, P.; Yan, R.; Fardy, M. Semiconductor Nanowire: What's Next? *Nano Lett.* **2010**, *10*, 1529–1536.
3. Wong, I. Y.; Almquist, B. D.; Melosh, N. A. Dynamic Actuation Using Nano-bio Interfaces. *Mater. Today* **2010**, *13*, 14–22.
4. Faraji, A. H.; Wipf, P. Nanoparticles in Cellular Drug Delivery. *Bioorg. Med. Chem.* **2009**, *17*, 2950–2962.
5. Xie, C.; Hanson, L.; Cui, Y.; Cui, B. Vertical Nanopillars for Highly Localized Fluorescence Imaging. *Proc. Natl. Acad. Sci. U. S. A.* **2011**, *108*, 3894–3899.
6. Xie, X.; Ma, D.; Zhang, L.-M. Fabrication and Properties of a Supramolecular Hybrid Hydrogel Doped with CdTe Quantum Dots. *RSC Adv.* **2015**, *5*, 58746–58754.
7. Duan, X.; Gao, R.; Xie, P.; Cohen-Karni, T.; Qing, Q.; Choe, H. S.; Tian, B.; Jiang, X.; Lieber, C. M. Intracellular Recordings of Action Potentials by an Extracellular Nanoscale Field-effect Transistor. *Nat. Nanotechnol.* **2012**, *7*, 174–179.

8. Salem, A. K.; Searson, P. C.; Leong, K. W. Multifunctional Nanorods for Gene Delivery. *Nat. Mater.* **2003**, *2*, 668–671.
9. Ma, D.; Xie, X.; Zhang, L.-M. A Novel Route to In-Situincorporation of Silver Nanoparticles into Supramolecular Hydrogel Networks. *J. Polym. Sci., Part B: Polym. Phys.* **2009**, *47*, 740–749.
10. Choi, Y.; Kim, K.; Hong, S.; Kim, H.; Kwon, Y.-J.; Song, R. Intracellular Protein Target Detection by Quantum Dots Optimized for Live Cell Imaging. *Bioconjugate Chem.* **2011**, *22*, 1576–1586.
11. Xie, X.; Xu, A. M.; Leal-Ortiz, S.; Cao, Y.; Garner, C. C.; Melosh, N. A. Nanostraw-Electroporation System for Highly Efficient Intracellular Delivery and Transfection. *ACS Nano* **2013**, *7*, 4351–4358.
12. Yum, K.; Wang, N.; Yu, M.-F. Nanoneedle: A Multifunctional Tool for Biological Studies in Living Cells. *Nanoscale* **2010**, *2*, 363–372.
13. Yan, R.; Park, J.-H.; Choi, Y.; Heo, C.-J.; Yang, S.-M.; Lee, L. P.; Yang, A. P. Nanowire-based Single-cell Endoscopy. *Nat. Nanotechnol.* **2012**, *7*, 191–196.
14. Singhal, R.; Orynbayeva, Z.; Sundaram, R. V. K.; Niu, J. J.; Bhattacharyya, S.; Vitol, E. A.; Schrlau, M. G.; Papazoglou, E. S.; Friedman, G.; Gogotsi, Y. Multifunctional Carbon-nanotube Cellular Endoscopes. *Nat. Nanotechnol.* **2011**, *6*, 57–64.
15. Xie, X.; Melosh, N. A. Fabrication of Sub-cell Size ″Spiky″ Nanoparticles and Their Interfaces with Biological Cells. *J. Mater. Chem. B* **2015**, *3*, 5155–5160.
16. Chen, X.; Kis, A.; Zettl, A.; Bertozzi, C. R. A Cell Nanoinjector Based on Carbon Nanotubes. *Proc. Natl. Acad. Sci. U. S. A.* **2007**, *104*, 8218–8222.
17. Na, Y.-R.; Kim, S. Y.; Gaublomme, J. T.; Shalek, A. K.; Jorgolli, M.; Park, H.; Yang, E. G. Probing Enzymatic Activity inside Living Cells Using a Nanowire–Cell "Sandwich" Assay. *Nano Lett.* **2013**, *13*, 153–158.
18. Obataya, I.; Nakamura, C.; Han, S.; Nakamura, N.; Miyake, J. Mechanical Sensing of the Penetration of Various Nanoneedles into a Living Cell using Atomic Force Microscopy. *Biosens. Bioelectron.* **2005**, *20*, 1652–1655.
19. Kim, W.; Ng, J. K.; Kunitake, M. E.; Conklin, B. R.; Yang, P. Interfacing Silicon Nanowires with Mammalian Cells. *J. Am. Chem. Soc.* **2007**, *129*, 7228–7229.
20. Hällström, W.; Mårtensson, T.; Prinz, C.; Gustavsson, P.; Montelius, L.; Samuelson, L.; Kanje, M. Gallium Phosphide Nanowires as a Substrate for Cultured Neurons. *Nano Lett.* **2007**, *7*, 2960–2965.
21. Berthing, T.; Sørensen, C. B.; Nygård, J.; Martinez, K. L. Applications of Nanowire Arrays in Nanomedicine. *J. Nanoneurosci.* **2009**, *1*, 3–9.
22. Shalek, A. K.; Robinson, J. T.; Karp, E. S.; Lee, J. S.; Ahn, D. R.; Yoon, M. H.; Sutton, A.; Jorgolli, M.; Gertner, R. S.; Gujral; et al. Vertical Silicon Nanowires as a Universal Platform for Delivering Biomolecules into Living Cells. *Proc. Natl. Acad. Sci. U. S. A.* **2010**, *107*, 1870–1875.
23. Shalek, A. K.; Gaublomme, J. T.; Wang, L.; Yosef, N.; Chevrier, N.; Andersen, M. S.; Robinson, J. T.; Pochet, N.; Neuberg, D.; Gertner, R. S.; et al. Nanowire-Mediated Delivery Enables Functional Interrogation of Primary Immune Cells: Application to the Analysis of Chronic Lymphocytic Leukemia. *Nano Lett.* **2012**, *12*, 6498–6504.
24. Yosef, N.; Shalek, A. K.; Gaublomme, J. T.; Jin, H.; Lee, Y.; Awasthi, A.; Wu, C.; Karwacz, K.; Xiao, S.; Jorgolli, M.; et al. Dynamic Regulatory Network Controlling TH17 Cell Differentiation. *Nature* **2013**, *496*, 461–468.
25. VanDersarl, J. J.; Xu, A. M.; Melosh, N. A. Nanostraws for Direct Fluidic Intracellular Access. *Nano Lett.* **2012**, *12*, 3881–3886.
26. Park, S.; Kim, Y.-S.; Kim, W. B.; Jon, S. Carbon Nanosyringe Array as a Platform for Intracellular Delivery. *Nano Lett.* **2009**, *9*, 1325–1329.
27. Peer, E.; Artzy-Schnirman, A.; Gepstein, L.; Sivan, U. Hollow Nanoneedle Array and Its Utilization for Repeated Administration of Biomolecules to the Same Cells. *ACS Nano* **2012**, *6*, 4940–4946.
28. Robinson, J. T.; Jorgolli, M.; Shalek, A. K.; Yoon, M.-H.; Gertner, R. S.; Park, H. Vertical Nanowire Electrode Arrays as a Scalable Platform for Intracellular Interfacing to Neuronal Circuits. *Nat. Nanotechnol.* **2012**, *7*, 180–184.
29. Xie, C.; Lin, Z.; Hanson, L.; Cui, Y.; Cui, B. Intracellular Recording of Action Potentials by Nanopillar Electroporation. *Nat. Nanotechnol.* **2012**, *7*, 185–190.
30. Robinson, J. T.; Jorgolli, M.; Park, H. Nanowire Electrodes for High-density Stimulation and Measurement of Neural Circuits. *Front. Neural Circuits* **2013**, *7*, 38.
31. Chiappini, C.; De Rosa, E.; Martinez, O.; Liu, X.; Steele, J.; Stevens, M. M.; Tasciotti, E. Biodegradable Silicon Nanoneedles Delivering Nucleic Acids Intracellularly Induce Localized *in Vivo* Neovascularization. *Nat. Mater.* **2015**, *14*, 532.
32. Berthing, T.; Bonde, S.; Rostgaard, K. R.; Madsen, M. H.; Sørensen, C. B.; Nygård, J.; Martinez, K. L. Cell Membrane Conformation at Vertical Nanowire Array Interface Revealed by Fluorescence Imaging. *Nanotechnology* **2012**, *23*, 415102.
33. Hanson, L.; Lin, Z. C.; Xie, C.; Cui, Y.; Cui, B. Characterization of the Cell–Nanopillar Interface by Transmission Electron Microscopy. *Nano Lett.* **2012**, *12*, 5815–5820.
34. Mumm, F.; Beckwith, K. M.; Bonde, S.; Martinez, K. L.; Sikorski, P. A Transparent Nanowire-Based Cell Impalement Device Suitable for Detailed Cell-Nanowire Interaction Studies. *Small* **2013**, *9*, 263–272.
35. Berthing, T.; Bonde, S.; Sørensen, C. B.; Utko, P.; Nygård, J.; Martinez, K. L. Intact Mammalian Cell Function on Semiconductor Nanowire Arrays: New Perspectives for Cell-Based Biosensing. *Small* **2011**, *7*, 640–647.
36. Lin, Z. C.; Xie, C.; Osakada, Y.; Cui, Y.; Cui, B. Iridium Oxide Nanotube Electrodes for Sensitive and Prolonged Intracellular Measurement of Action Potentials. *Nat. Commun.* **2014**, *5*, 3206.
37. Xie, X.; Xu, A. M.; Angle, M. R.; Tayebi, N.; Verma, P.; Melosh, N. A. Mechanical Model of Vertical Nanowire Cell Penetration. *Nano Lett.* **2013**, *13*, 6002–6008.
38. Cuvelier, D.; Théry, M.; Chu, Y.-S.; Dufour, S.; Thiéry, J.-P.; Bornens, M.; Nassoy, P.; Mahadevan, L. The Universal Dynamics of Cell Spreading. *Curr. Biol.* **2007**, *17*, 694–699.
39. Zhang, X.; Jiang, G.; Cai, Y.; Monkley, S. J.; Critchley, D. R.; Sheetz, M. P. Talin Depletion Reveals Independence of Initial Cell Spreading from Integrin Activation and Traction. *Nat. Cell Biol.* **2008**, *10*, 1062–1068.
40. May, R. C.; Dubin-Thaler, B. J.; Hofman, J. M.; Cai, Y.; Xenias, H.; Spielman, I.; Shneidman, A. V.; David, L. A.; Döbereiner, H.-G.; Wiggins, C. H.; et al. Quantification of Cell Edge Velocities and Traction Forces Reveals Distinct Motility Modules during Cell Spreading. *PLoS One* **2008**, *3*, e3735.
41. Pietuch, A.; Janshoff, A. Mechanics of Spreading Cells Probed by Atomic Force Microscopy. *Open Biol.* **2013**, *3*, 130084–130084.
42. Carey, S. P.; Charest, J. M.; Reinhart-King, C. A. Forces During Cell Adhesion and Spreading: Implications for Cellular Homeostasis. *Stud. Mechanobiol. Tissue Eng. Biomater.* **2010**, *4*, 29–69.
43. Qi, S.; Yi, C.; Ji, S.; Fong, C.-C.; Yang, M. Cell Adhesion and Spreading Behavior on Vertically Aligned Silicon Nanowire Arrays. *ACS Appl. Mater. Interfaces* **2009**, *1*, 30–34.
44. Wolfe, J.; Steponkus, P. L. Mechanical Properties of the Plasma Membrane of Isolated Plant Protoplasts. *Plant Physiol.* **1983**, *71*, 276–285.
45. Wolfe, J.; Dowgert, M. F.; Steponkus, P. L. Dynamics of Incorporation of Material into the Plasma Membrane and the Lysis of Protoplasts during Rapid Expansions in Area. *J. Membr. Biol.* **1985**, *86*, 127–138.
46. Wolfe, J.; Dowgert, M. F.; Steponkus, P. L. Mechanical Study of the Deformation and Rupture of the Plasma Membranes of Protoplasts during Osmotic Expansions. *J. Membr. Biol.* **1986**, *93*, 63–74.
47. Ehrenstein, D.; Iwasa, K. H. Viscoelastic Relaxation in the Membrane of the Auditory Outer Hair Cell. *Biophys. J.* **1996**, *71*, 1087–1094.
48. Batcheldera, E. L.; Hollopeterd, G.; Campilloa, C.; Mezangesa, X.; Jorgensen, E. M.; Nassoya, P.; Sensg, P.; Plastinoa, J. Membrane Tension Regulates Motility by Controlling

Lamellipodium Organization. *Proc. Natl. Acad. Sci. U. S. A.* **2011**, *108*, 11429–11434.
49. Gauthier, N. C.; Fardin, M. A.; Roca-Cusachs, P.; Sheetz, M. P. Temporary Increase in Plasma Membrane Tension Coordinates the Activation of Exocytosis and Contraction during Cell Spreading. *Proc. Natl. Acad. Sci. U. S. A.* **2011**, *108*, 14467–14472.
50. Santoro, F.; Dasgupta, S.; Schnitker, J.; Auth, T.; Neumann, E.; Panaitov, G.; Gompper, G.; Offenhausser, A. Interfacing Electrogenic Cells with 3D Nanoelectrodes: Position, Shape, and Size Matter. *ACS Nano* **2014**, *8*, 6713–6723.
51. Xu, A. M.; Aalipour, A.; Leal-Ortiz, S.; Mekhdjian, A. H.; Xie, X.; Dunn, A. R.; Garner, C. C.; Melosh, N. A. Quantification of Nanowire Penetration into Living Cells. *Nat. Commun.* **2014**, *5*, 2041–1723.
52. Verma, P.; Wong, I. Y.; Melosh, N. A. Continuum Model of Mechanical Interactions between Biological Cells and Artificial Nanostructures. *Biointerphases* **2010**, *5*, 37–44.
53. Skalak, R.; Tozeren, A.; Zarda, R. P.; Chien, S. Strain Energy Function of Red Blood Cell Membranes. *Biophys. J.* **1973**, *13*, 245–264.
54. Evans, E. A. A New Material Concept for the Red Cell Membrane. *Biophys. J.* **1973**, *13*, 926–940.
55. Kagiwada, H.; Nakamura, C.; Kihara, T.; Kamiishi, H.; Kawano, K.; Nakamura, N.; Miyake, J. The Mechanical Properties of a Cell, as Determined by Its Actin Cytoskeleton, Are Important for Nanoneedle Insertion into a Living cell. *Cytoskeleton* **2010**, *67*, 496–503.
56. Evans, E. A.; Waugh, R.; Melnik, L. Elastic Area Compressibility Modulus of Red Cell Membrane. *Biophys. J.* **1976**, *16*, 586–595.
57. Lulevich, V.; Zimmer, C. C.; Hong, H.; Jin, L.; Liu, G. Single-Cell Mechanics Provides a Sensitive and Quantitative Means for Probing Amyloid-peptide and Neuronal Cell Interactions. *Proc. Natl. Acad. Sci. U. S. A.* **2010**, *107*, 13872–13877.
58. Sen, S.; Subramanian, S.; Discher, D. E. Indentation and Adhesive Probing of a Cell Membrane with AFM: Theoretical Model and Experiments. *Biophys. J.* **2005**, *89*, 3203–3213.
59. Tan, S. C. W.; Yang, T.; Gong, Y.; Liao, K. Rupture of Plasma Membrane under Tension. *J. Biomech* **2011**, *44*, 1361–1366.
60. Evans, E.; Heinrich, V.; Ludwig, F.; Rawiczy, W. Dynamic Tension Spectroscopy and Strength of Biomembranes. *Biophys. J.* **2003**, *85*, 2342–2350.
61. Yang, W. H.; Hsu, K. H. Indentation of a Circular Membrane. *J. Appl. Mech.* **1971**, *38*, 227–230.
62. Simson, R.; Wallraff, E.; Faix, J.; Niewöhner, J.; Gerisch, G.; Sackmann, E. Membrane Bending Modulus and Adhesion Energy of Wild-type and Mutant Cells of Dictyostelium Lacking Talin or Cortexillins. *Biophys. J.* **1998**, *74*, 514–522.
63. Sackmann, E.; Bruinsma, R. Cell Adhesion as Wetting Transition? *ChemPhysChem* **2002**, *3*, 262–269.
64. Hategan, A.; Law, R.; Kahn, S.; Discher, D. E. Adhesively-Tensed Cell Membranes: Lysis Kinetics and Atomic Force Microscopy Probing. *Biophys. J.* **2003**, *85*, 2746–2759.
65. Cojoc, D.; Difato, F.; Ferrari, E.; Shahapure, R. B.; Laishram, J.; Righi, M.; Fabrizio, E. M. D.; Torre, V. Properties of the Force Exerted by Filopodia and Lamellipodia and the Involvement of Cytoskeletal Components. *PLoS One* **2007**, *2*, e1072.
66. Shahapure, R.; Difato, F.; Laio, A.; Bisson, G.; Ercolini, E.; Amin, L.; Ferrari, E.; Torre, V. Force Generation in Lamellipodia Is a Probabilistic Process with Fast Growth and Retraction Events. *Biophys. J.* **2010**, *98*, 979–988.
67. Hällström, W.; Lexholm, M.; Suyatin, D. B.; Hammarin, G.; Hessman, D.; Samuelson, L.; Montelius, L.; Kanje, M.; Prinz, C. N. Fifteen-Piconewton Force Detection from Neural Growth Cones Using Nanowire Arrays. *Nano Lett.* **2010**, *10*, 782–787.
68. Yang, M. T.; Sniadecki, N. J.; Chen, C. S. Geometric Considerations of Micro- to Nanoscale Elastomeric Post Arrays to Study Cellular Traction Forces. *Adv. Mater.* **2007**, *19*, 3119–3123.
69. Tieleman, D. P.; Leontiadou, H.; Mark, A. E.; Marrink, S.-J. Simulation of Pore Formation in Lipid Bilayers by Mechanical Stress and Electric Fields. *J. Am. Chem. Soc.* **2003**, *125*, 6382–6383.
70. Angle, M. R.; Wang, A.; Thomas, A.; Schaefer, A. T.; Melosh, N. A. Penetration of Cell Membranes and Synthetic Lipid Bilayers by Nanoprobes. *Biophys. J.* **2014**, *107*, 2091–2100.